Electrochemical performance of KTiOAsO$_4$ (KTA) in potassium-ion batteries from density-functional theory

A. Bocchini [1,*] U. Gerstmann [1] T. Bartley [1] H.-G. Steinrück [2] G. Henkel, [1] and W. G. Schmidt [1]

[1]*Department Physik, Universität Paderborn, 33095 Paderborn, Germany*
[2]*Department Chemie, Universität Paderborn, 33095 Paderborn, Germany*

The electrochemical performance of potassium titanyl arsenate (KTiOAsO$_4$, KTA) as the cathode and anode in K-ion batteries is calculated within density-functional theory. Cathodes and anodes are modeled using K-deficient K$_{1-x}$TiOAsO$_4$ ($x = 0.0$–1.0) and K-doped KTiOAsO$_4$K$_x$ ($x = 0.0$–0.5), respectively. For KTA cathodes/anodes a slightly larger/smaller open circuit voltage is found than predicted for potassium titanyl phosphate. The present results suggest that a solely KTA-based K-ion battery can reach an average working voltage of about 3.8 V. The migration barriers of K vacancies and K dopants are found to be smaller than 750 meV. In addition, the present calculations show a very moderate volume expansion and shrinkage upon K intercalation and deintercalation. Our results suggest KTA to be a promising electrode material for K-ion batteries.

I. INTRODUCTION

There is an increasing effort to replace fossil fuels by renewable energies such as solar, tidal, or wind energy. This is accompanied by the need for efficient energy storage. Li-ion batteries (LIBs) combine good charging efficiencies with high-energy densities and low self-discharge rates [1–3]. In addition, under special conditions, they are rechargeable several thousand charging cycles without any significant deterioration [4].

Still, there is an ongoing search for alternative technologies [5–10]. In this context, Na-ion (NIB) and K-ion (KIB) batteries appear as promising candidates [6,11–16]. Both alkali metals show similar chemical properties as Li. However, due to their larger ionic radii, new electrode materials have to be explored.

Potassium titanyl phosphate (KTiOPO$_4$, KTP) has been suggested as an excellent material as both a cathode [9] and anode [10,17–19]. In the cathode material, K vacancies are generated during operation, and Ti-Ti coordinated O atoms near the vacancy oxidize [9]. The application as an anode requires the intercalation of additional K atoms, which causes the reduction of Ti atoms [10]. However, upon reduction of Ti atoms in the vicinity of O vacancies, KTP is known to be affected by the so-called gray tracking [20–22]. Gray tracks are a characteristic material damage, which forms for example upon exposure to intense light or electric fields and

*adrianab@mail.upb.de

manifests itself by dark spots in the crystal. Their formation is accompanied by an increased absorption for laser light at 532 and 1064 nm [23–27]. However, this phenomenon may also be detrimental for battery applications: The Ti^{3+} centers instrumental for the gray tracks' formation are thermally stable [20], and electrons are likely to be trapped by Ti atoms in the vicinity of O vacancies rather than far from them [21]. Thus, they may affect the electron flux.

This suggests to study further members of the KTP-type crystal family with promising electrochemical properties [5,18,28–34]. In particular, potassium titanyl arsenate (KTA, KTiOAsO$_4$) is interesting in this context, as it is more robust against the formation of gray tracks than KTP [35]. The crystal is already well established in (non)linear optics. In fact, the material features, e.g., high chemical and thermally stabilities as well as high nonlinear optical coefficients, good conversion efficiencies, a broad transparency range, and a high ionic conductivity [36–39]. Its large band gap [40], however, will require material processing, e.g., coating with electroconducting carbon, in order to realize sufficient electrode conductivity [10,41].

In the present paper we use density-functional theory calculations in order to test the suitability of KTA as a cathode and anode for potassium-ion batteries (KIBs).

II. COMPUTATIONAL DETAILS

The density-functional-theory (DFT) calculations are performed using the open-source QUANTUM ESPRESSO package [42,43]. The electron-ion interactions are modeled via norm-conserving pseudopotentials, treating Ti $3s^2\,3p^3\,3d^3\,4s^1$, As $4s^2\,4p^3$, K $4s^1$, and O $2s^2\,2p^4$ states as valence electrons. The electron exchange and correlation (XC) is described within the generalized gradient approximation (GGA) using the revised Perdew-Burke-Ernzerhof functional PBEsol [44].

DFT calculations using (semi)local functionals are known to systematically underestimate redox voltages. A better description can be achieved by applying hybrid functionals, which provide quantitatively correct voltages [45]. Unfortunately, hybrid DFT is too expensive to be routinely applied to a large number of complex structures. The Hubbard correction scheme, however, provides reliable intercalation voltages and anionic oxidation [45,46–50] at a much lower computational cost. This methodology has been applied in the present work. In detail, we followed the approach by Cococcioni and de Gironcoli [51] and used a Hubbard correction of $U = 5.8$ eV for the Ti $3d$ states. This value has been determined self-consistently by adding a small positive and a small negative potential shift on each nonequivalent Hubbard site and by computing the variation of the occupation of all sites in the supercell once allowing the self-consistent readjustment of the Kohn-Sham potential to screen the localized perturbation and once disallowing for this screening [51]. This procedure allows for an accurate description of occupied midgap Ti $3d$ defect states that result from the reduction of Ti atoms after the K intercalation in the anode. In order to determine the error bar associated with the PBEsol $+ U$ methodology, we compared the results for a KTA unit cell with one deintercalated K atom with hybrid PBE0 [52] calculations. The calculated voltages obtained from Eq. (4) agree within 0.3 V.

During geometry optimization, the atomic positions and the lattice parameters are relaxed until total energy fluctuations and residual forces are below 10^{-8} Ry and 10^{-4} Ry/bohrs, respectively. The electron wave functions are expanded into plane waves up to an energy cutoff of 100 Ry.

KTA crystallizes in an orthorhombic lattice with space group $Pna2_1$. The 64-atom unit cell contains eight formula units of KTiOAsO$_4$. Its calculated equilibrium lattice parameters of $a = 13.412$ Å, $b = 6.777$ Å, and $c = 10.834$ Å agree well with the experimental data $a = 13.129$ Å, $b = 6.577$ Å, and $c = 10.786$ Å [53]. Here, the Baldereschi point [54] is used to sample the KTA Brillouin zone. The diffusion of K dopants and K vacancies is modeled using the nudged elastic band (NEB) method [55]. In the NEB calculations, a force convergence criterion of 0.05 eV/Å is used. Further details on modeling the cathode and anode material are given in Secs. III A and IV A, respectively.

The following two reactions take place at the cathode and anode, respectively, during the KIB charging,

$$\text{KTiOAsO}_4 \longrightarrow \text{K}_{1-x}\text{TiOAsO}_4 + x(\text{K}^{+1} + e^-), \quad (1)$$

$$\text{KTiOAsO}_4 + x(\text{K}^{+1} + e^-) \longrightarrow \text{KTiOAsO}_4\text{K}_x. \quad (2)$$
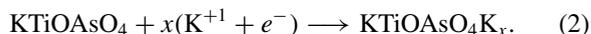
Here, x is the concentration of (de)intercalated K per formula unit.

The average voltage ($\overline{V}$) is an essential parameter to describe the performance of the electrode materials. A high $\overline{V}$ for the cathode material and a low $\overline{V}$ for the anode material [9,10] are required for a high working voltage. The $\overline{V}$ is obtained from the change in Gibbs' free energy upon K (de)intercalation as

$$\overline{V} = \pm \frac{\Delta G}{zF}, \quad (3)$$
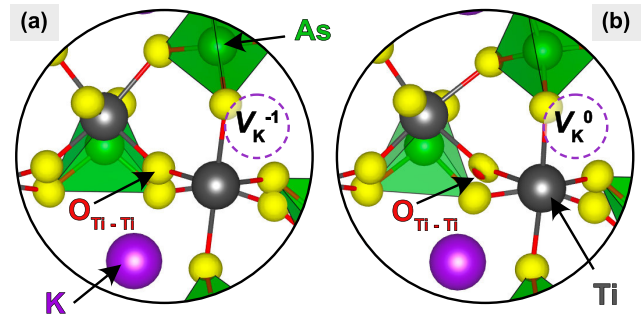
FIG. 1. Electron charge density (yellow isosurface) in the vicinity of the negatively charged V_{K}^{-1} (a) and neutral vacancy V_{K}^{0} (b). The Ti-Ti coordinated O atom (O$_{\text{Ti-Ti}}$) oxidizes subsequent to excess electron removal.

where positive and negative signs refer to cathode and anode materials, respectively, F is the Faraday constant, and z is the transferred charge [10,56–61]. Note that the Gibbs' free energy refers to reactions (1) and (2) and their explicit directions. In the present calculations, temperature and volume effects are neglected and the Gibbs' free-energy changes are approximated by $\Delta G \approx \Delta E$ with ΔE as the internal energy. Thus Eq. (3) reads

$$\overline{V} \approx \pm \frac{\Delta E}{zF}. \quad (4)$$

Since, however, the transferred charge is equal to the concentration x of (de)intercalated K, it is possible to set $z = xe_0$ and Eq. (4) reads

$$\overline{V} \approx \pm \frac{\Delta E}{zF} = \frac{E_{\text{(de)in}}}{e_0 F}, \quad (5)$$

with e_0 as the elementary charge and $E_{\text{(de)in}} = \Delta E / x$ as the K (de)intercalation energy (also see Secs. III A and IV A).

In order to guarantee a robust long-term operation, electrodes should not suffer from strong deformations upon K-ion intercalation or deintercalation. Based on the energetics of
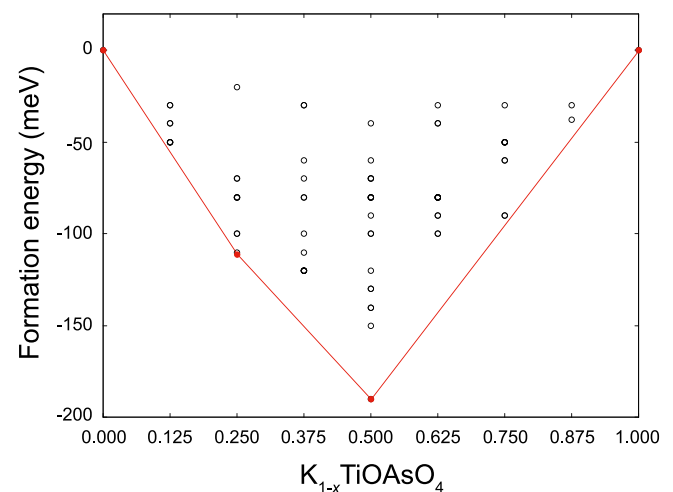
FIG. 2. Formation energy E_f vs the concentration x of deintercalated K. The red line (i.e., the convex hull) connects all stable ordered phases.
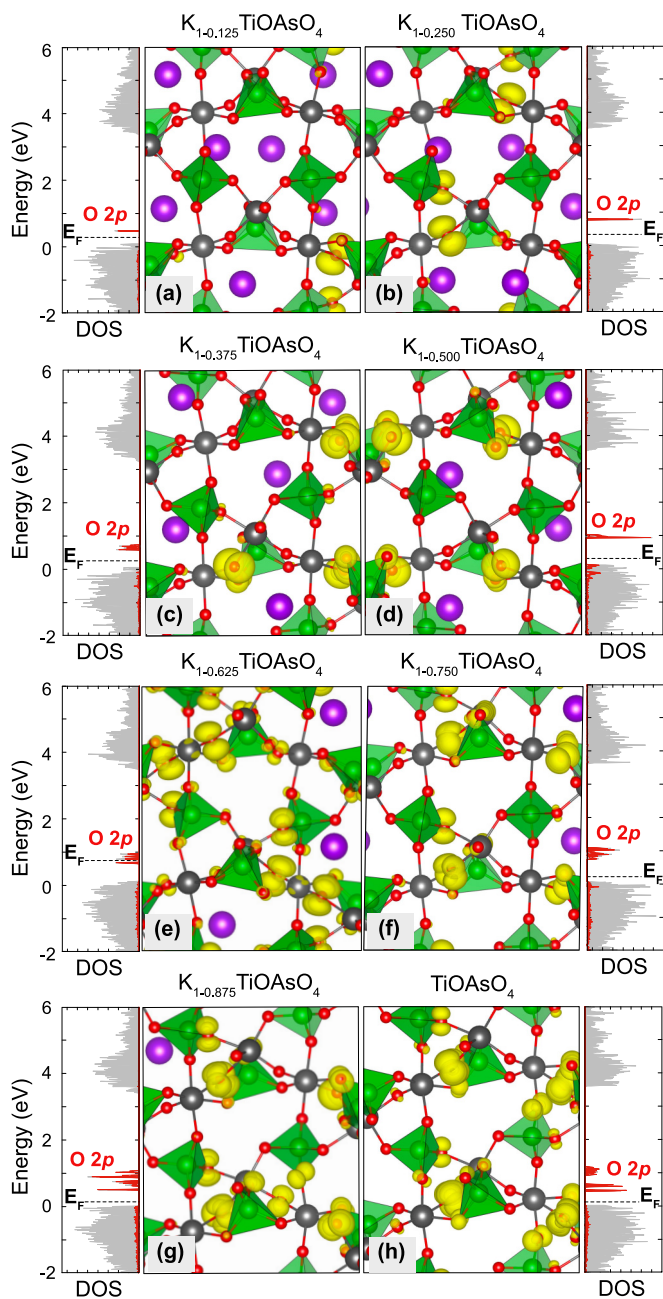
FIG. 3. Electronic orbitals of the midgap defect levels and electronic DOS of the most stable K$_{1-x}$TiOAsO$_4$ configurations calculated here. The position of the Fermi level is indicated, too.

the K excess and deficiency material, the average volume expansion or shrinkage is computed here assuming a Boltzmann distribution of the defect structures that realize a specific stoichiometry.

Finally, the gravimetric capacity C of the electrodes [10] is determined from

$$C = \frac{xF}{M_x}, \qquad (6)$$

where M_x is the molar mass of one formula unit of K$_{1-x}$TiOAsO$_4$ (KTiOAsO$_4$K$_x$) and F the Faraday constant.
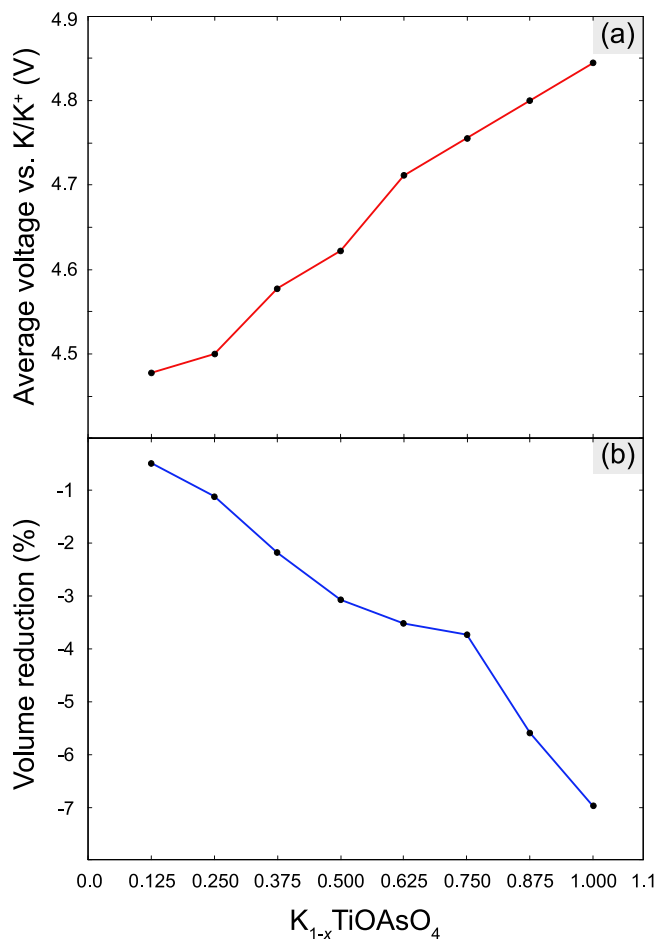
FIG. 4. Average voltage (a) and volume reduction (b) of K$_{1-x}$TiOAsO$_4$ with $x = 0.125$–1.

III. CATHODE MATERIAL

A. Models

In order to model KTA as a cathode material, K-deficient K$_{1-x}$TiOAsO$_4$ ($x = 0.125$–1) is considered by deintercalating up to 8 K ions from the unit cell. Similar to KTP, the deintercalation of a neutral K atom is accompanied by the formation of a hole at the valence band maximum (VBM) [62]. Therefore, in thermodynamic equilibrium, K vacancies are energetically stable only in the charge state −1. The extra charge is mainly trapped by one of the Ti-Ti coordinated O atoms (O$_{\text{Ti-Ti}}$) near the vacancy [see Fig. 1(a)]. For the computational modeling of V_K^0 we proceed in two steps: First, the geometry of the negatively charged vacancy V_K^{-1} is optimized. Second, the excess electron is removed and the structure is relaxed again. In order to simulate noninteracting defects, spin-polarized calculations are performed, where the total spin angular momentum is $S = \frac{n}{2}$. Here, $n = 1$–8 corresponds to the number of deintercalated K atoms in the unit cell. This method allows for an accurate description of the oxidation of the nearest Ti-Ti coordinated O atom [also see Fig. 1(a) versus Fig. 1(b)]. There are 256 possible configurations. Some of them, however, are related by symmetry. The stable configurations are determined here from a convex hull construction [9,63]. Here, the formation
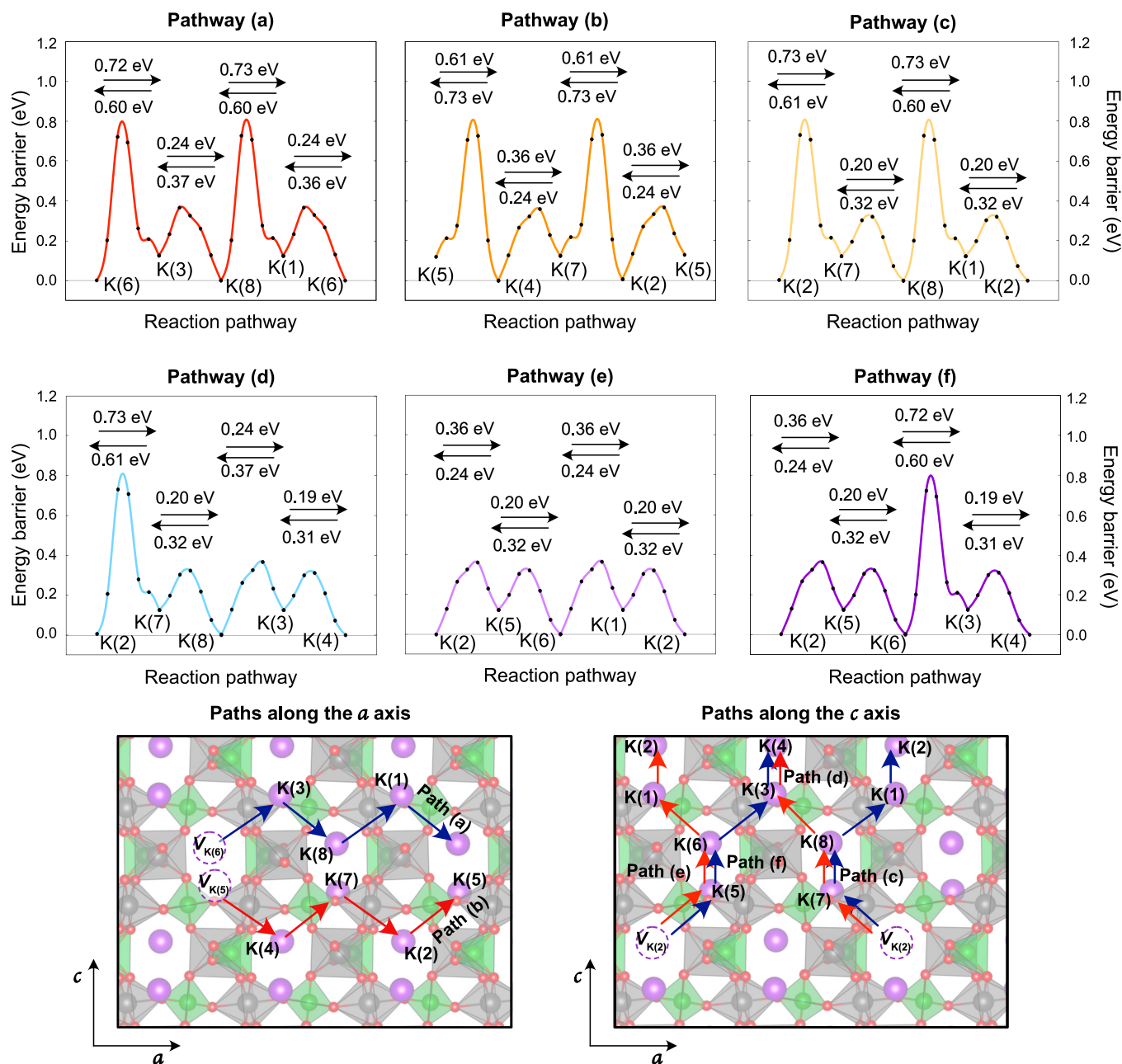
FIG. 5. Schematic representation of two K-vacancy migration along the *a* axis [pathways (a) and (b)] and four along the *c* axis [pathways (c)–(f)] together with the corresponding energy barriers. The activation energies of each segment are indicated.

energy E_f,

$$E_f = E_{\mathrm{K}_{1-x}\mathrm{TiOAsO}_4} - (1-x) \cdot E_{\mathrm{KTiOAsO}_4} - x \cdot E_{\mathrm{TiOAsO}_4}, \quad (7)$$

is considered, where $E_{\mathrm{K}_{1-x}\mathrm{TiOAsO}_4}$ is the total energy of $\mathrm{K}_{1-x}\mathrm{TiOAsO}_4$, and E_{KTiOAsO_4} and E_{TiOAsO_4} refer to the respective energies of stoichiometric $\mathrm{KTiOAsO}_4$ and TiOAsO_4 per formula unit. The so calculated values are compiled in Fig. 2. The convex hull corresponds to the red line, which connects the lowest-energy ordered phases. The phases with formation energy above this curve are unstable with respect to a mixed-phase system composed of the structures which delimit the start and the end point of the underlying tie line. As can be seen, at zero temperature only the vacancy concentrations $x = 0.00$, 0.25, 0.50, and 1.00 correspond to stable

phase. However, the energy deviations of the phases with $x = 0.125$, 0.750, and 0.875 from the convex hull are small, below 10 meV. Therefore, these phases can be expected to be realized at finite temperatures due to entropy effects. On the other hand, for $0.25 < x < 0.50$ and $0.50 < x < 0.75$ phase separation may occur.

The energetically most favorable vacancy configurations together with the corresponding electronic density of states (DOS) for all stoichiometries considered are shown in Fig. 3. Obviously, the K deintercalation does not have a strong influence on the atomic structural of the TiOAsO_4 matrix. In fact, it is essentially preserved. However, the K atoms that remain in the matrix rearrange. Even if all K atoms are deintercalated, only a negligible distortion in conjunction with a volume

shrinkage below 7% is calculated [see Fig. 4(b)]. The volume shrinkage calculated here for KTA is larger than the 1.5% predicted for KTP [9], but below the value 7.8% predicted for KVPO$_4$F [9].

The electronic DOS shown in Fig. 3 demonstrates that the K deintercalation gives rise to O 2p defect states in the band gap, which originate from two distinct O atoms near the vacancy. One of these O atoms, more precisely the one coordinated to two Ti atoms (O$_{Ti-Ti}$ in Fig. 1), is slightly oxidized. The defect levels are partially occupied or totally empty depending on the vacancy configuration.

The K deintercalation energy E_{dein} of each computed structure has been calculated via [9]

$$E_{dein} = \frac{E_{K_{1-x}TiOAsO_4} - E_{KTiOAsO_4} + x \cdot E_K}{x}, \qquad (8)$$

where $E_K = -0.82$ eV is the energy of a K atom in metallic K. We find that for the removal of each K atom a deintercalation energy between 4.5 and 4.8 eV has to be applied to the system. This value is of the same order of magnitude, albeit slightly larger that calculated for KTP (between about 4.2 and 4.6 eV) [9]. A positive deintercalation energy implies that energy has to be applied to the system in order to create the vacancy, corresponding to battery charging.

In Fig. 4(a) the average voltage based on all K$_{1-x}$TiOAsO$_4$ structures considered for a specific K-vacancy concentration x is shown depending on the stoichiometry. The average voltage rises steadily with the concentration x. It assumes values between 4.47 V for $x = 0.125$ and 4.80 V for $x = 1$, i.e., when all K are removed from the cell. Due to the higher molar mass of As compared to P, KTA shows a lower gravimetric capacity than KTP: While the capacity of the latter can reach 168.73 mAh g^{-1} when all the K atoms are removed from the cell [9], the maximum capacity of KTA amounts to 132.17 mAh g^{-1}. As a consequence, the gravimetric energy density of KTA is lower than that of KTP, but it is very close to that of KVPO$_4$F, i.e., 634.57 Wh/kg, 774.46 Wh/kg [9], and 664.68 Wh/kg [9], respectively.

B. K-vacancy diffusion

Besides a high (or rather low) average voltage and high capacity, a good electrode should feature low diffusion barriers to facilitate ion (de)intercalation. In order to investigate the vacancy diffusion mechanisms, we perform NEB calculations along the a and c direction of the crystal. In KTP family member compounds, the diffusion along the b axis was found to be unfavorable [5]. Therefore, this pathway was discarded here. We explore the migration of a single K vacancy (i.e., $x = 0.125$) along two different pathways along the a axis and four different pathways along the c axis of the material. The energy barriers together with a schematic representation of the chosen pathways are shown in Fig. 5. All paths are characterized by relatively low activation energies between 0.19 and 0.73 eV. Although these values are slightly higher than the activation energies of the Rb$^+$ migration in RbVPO$_4$F [5], and those reported for KTP [9], they are still low enough to guarantee a fast K deintercalation. The fact that the activation energy for vacancy diffusion is locally smaller for migration in the $-a$ and $-c$ directions than in the opposite direction
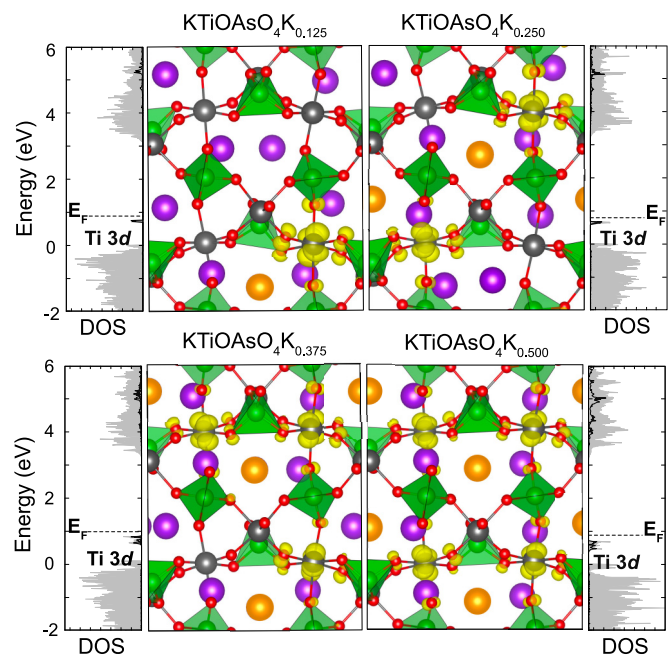
FIG. 6. Electronic orbitals of the midgap defect levels and electronic DOS of the most stable KTiOAsO$_4$K$_x$ configurations calculated here. K lattice sites are marked in purple, and K intercalation sites are marked in orange. The position of the Fermi level is indicated, too.

is related to the intrinsic polarization of the crystal. In addition, we find that the optimal diffusion pathway corresponds to the anticlockwise spiral pathway along the $-c$ axis, i.e., K(2) $\longrightarrow$ K(5) $\longrightarrow$ K(6) $\longrightarrow$ K(1) $\longrightarrow$ K(2), i.e., pathway (e) in Fig. 5, which is characterized by activation energies lower than 0.33 eV.

IV. ANODE MATERIAL

A. Models

Modeling KTA as an anode material requires the intercalation of K atoms. In the case of KTP, eight different intercalations sites were identified [10]. These sites have been probed here for KTA. The AsO$_4$ tetrahedra in KTA, however, are larger than the corresponding PO$_4$ units in KTP. This renders the intercalation in the KTP intercalation sites unfavorable and reduces the number of potential K positions to the four sites shown in Fig. 6. These correspond to the intercalation sites $M1$–$M4$ in Ref. [9] shifted along the $-b$ direction by about 25% of the lattice parameter. Consequently, we simulate KTiOAsO$_4$K$_x$ here for the range $x = 0.125$–0.5, where x is the number of intercalated K per formula unit. All 15 possible combinations of intercalations sites have been simulated. In analogy to the cathode calculations, neutral interstitials have to be considered. The total spin angular momentum was set to $S = \frac{n}{2}$, where $n = 1$–4 corresponds to the number of intercalated K atoms per unit cell.

The intercalation of each K atom causes the reduction of a Ti^{4+} into Ti^{3+} in its vicinity. This can be seen (i) from the formation of occupied midgap Ti-3d defect levels, and (ii) from the defect levels' contribution to the wave function to the
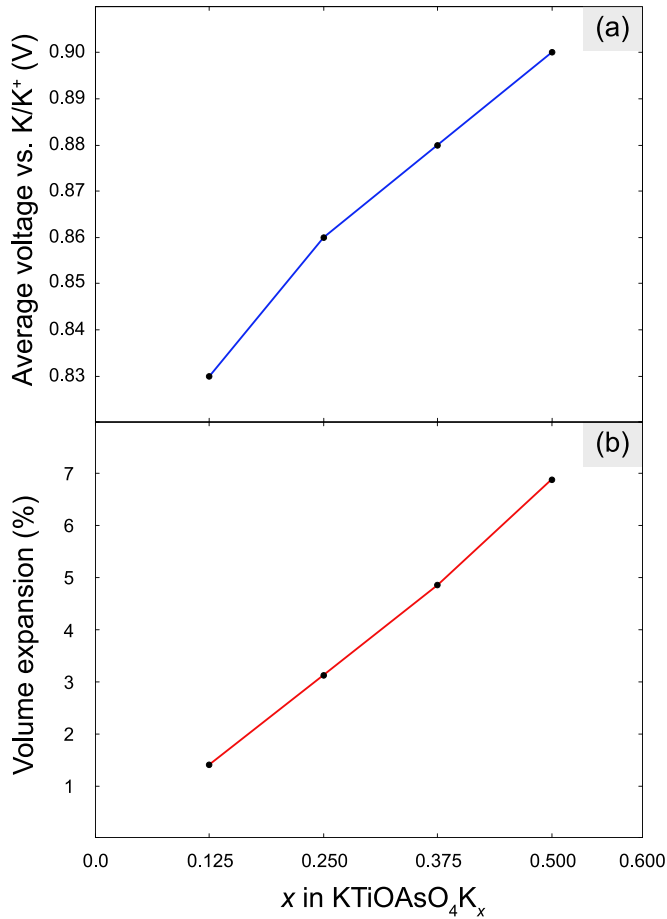
FIG. 7. Average voltage (a) and volume reduction (b) of $K_{1-x}TiOAsO_4$ with $x = 0.125$–0.5.

FIG. 8. Schematic representation of the four possible K-ion migration pathways along the c axis together with the corresponding energy barriers. The activation energies of each segment are indicated. Along the paths, K interstitials [$K_i(i)$ are marked in orange, and K lattice sites [$K(j)$] are marked in purple.

charge density (see Fig. 6). Note that in Fig. 6 only the energetically most favorable configuration for each concentration is shown.

The intercalation energy E_{in} associated with the K intercalation is obtained as [64]

$$E_{in} = \frac{E_{KTiOAsO_4K_x} - E_{KTiOAsO_4} - x \cdot E_K}{x}, \qquad (9)$$

where $E_{KTiOAsO_4K_x}$ is the energy of a formula unit of $KTiOAsO_4K_x$. As x increases, the intercalation energy per K interstitial varies between -0.8 and -0.2 eV. It is always negative, i.e., K atoms will spontaneously intercalate in the anode.

The average voltage and volume expansion of the four different concentrations x of intercalated K are shown in Figs. 7(a) and 7(b), respectively. As the concentration of intercalated K increases, both the average voltage and the volume expansion with respect to pristine KTA increase. The former varies between 0.83 and 0.90 V, the latter between 1.41% and 6.89%. Thus, KTA shows a slightly lower average voltage and a similar volume expansion as KTP [10] after the intercalation of the same amount of K. Regarding the gravimetric capacity, we calculate values between 51.26 mAh g^{-1} (i.e., for $x = 0.5$) leading to gravimetric energy densities between 11.32 and 46.37 Wh/kg. Again, due to the higher molar mass of As compared to P, the capacity of KTA is lower than that of KTP

(between 16.52 and 61.61 mAh g^{-1} for the same concentration of intercalated K) [10].

B. K-ion diffusion

In the previous section it was shown that the electrochemical properties of KTA are comparable to those of KTP. Next, we compare the K-ion diffusion in KTA and KTP. We perform NEB calculations to investigate the diffusion mechanisms of a single K_i.

Due to the peculiar positioning of the K interstitials within the crystal lattice, a direct K-ion migration along the a axis is hindered by the TiO$_6$-PO$_4$ chains. Thus, these pathways will not be considered here. For the computation of the migration along the b axis, the $KTiOAsO_4K_{0.125}$ unit cell has to be

doubled along this direction. In fact, the K ion migrates from one intercalation site into the equivalent position of an adjacent cell. Surprisingly, despite the large channel, we found a rather unfavorable activation energy of 1.91 eV.

Regarding the ion migration along the c axis, we simulate four different pathways (see Fig. 8). Along every pathway, the K$_i$ migrates through the cell between intercalation and intrinsic lattice sites. The activation energies for ion migration do not depend on the direction one path is traversed. We find that the energy barriers of different paths are very close in energy (all below 0.76 eV). Note that this values are smaller than those found for the K-ion migration in KTP crystals along the a axis [10]. The optimal diffusion pathway is again the one corresponding to the anticlockwise spiral along the c axis of the crystal, i.e., K$_i$(3) $\longrightarrow$ K(2) $\longrightarrow$ K(5) $\longrightarrow$ K$_i$(2) $\longrightarrow$ K(6) $\longrightarrow$ K(1) $\longrightarrow$ K$_i$(3) [see pathway (d) in Fig. 8]. This path describes thus the generally preferred movement for both ions and vacancies.

V. CONCLUSION

In this paper, the performance of KTA as both the cathode and anode for K-ion batteries has been systematically studied using density-functional theory.

We found that KTA combines a high average working voltage (about 3.8 V) with a relatively small volume deformation, at least for moderate concentrations of K vacancies (intercalated K). Moreover, also the gravimetric energy densities of the material are in the same order of those of other members of the KTP-type crystal family. In addition, the dynamics of the K-vacancy (K-ion) migration computed via NEB calculations revealed that both mechanisms are characterized by low activation energies for all studied diffusion pathways.

The present results suggest that KTA may be a promising material to be used as a cathode as well as an anode in K-ion batteries. A KIB design in which both electrodes are composed of KTA could reach working voltages up to 4.0 V.

[1] J. B. Goodenough and K.-S. Park, J. Am. Chem. Soc. **135**, 1167 (2013).

[2] B. Dunn, H. Kamath, and J.-M. Tarascon, Science **334**, 928 (2011).

[3] M. Li, J. Lu, Z. Chen, and K. Amine, Adv. Mater. **30**, 1800561 (2018).

[4] J. E. Harlow, X. Ma, J. Li, E. Logan, Y. Liu, N. Zhang, L. Ma, S. L. Glazier, M. M. E. Cormier, M. Genovese, S. Buteau, A. Cameron, J. E. Stark, and J. R. Dahn, J. Electrochem. Soc. **166**, A3031 (2019).

[5] S. S. Fedotov, A. S. Samarin, V. A. Nikitina, D. A. Aksyonov, S. A. Sokolov, A. Zhugayevych, K. J. Stevenson, N. R. Khasanova, A. M. Abakumov, and E. V. Antipov, J. Mater. Chem. A **6**, 14420 (2018).

[6] K. Kubota, M. Dahbi, T. Hosaka, S. Kumakura, and S. Komaba, Chem. Rec. **18**, 459 (2018).

[7] H. Kim, J. C. Kim, M. Bianchini, D.-H. Seo, J. Rodriguez-Garcia, and G. Ceder, Adv. Energy Mater. **8**, 1702384 (2018).

[8] T. Hosaka, K. Kubota, A. S. Hameed, and S. Komaba, Chem. Rev. **120**, 6358 (2020).

[9] J. Huang, X. Cai, H. Yin, Y. Li, W. Lin, S. Huang, and Y. Zhang, J. Phys. Chem. Lett. **12**, 2721 (2021).

[10] J. Huang, X. Cai, Y. Li, Z. Fang, Y. Li, W. Lin, S. Huang, and Y. Zhang, J. Chem. Phys. **156**, 204702 (2022).

[11] J. Hao, K. Xiong, J. Zhou, A. M. Rao, X. Wang, H. Liu, and B. Lu, Energy Environ. Mater. **5**, 261 (2022).

[12] H. Ding, J. Zhou, A. M. Rao, and B. Lu, Natl. Sci. Rev. **8**, nwaa276 (2020).

[13] D. Su, A. McDonagh, S.-Z. Qiao, and G. Wang, Adv. Mater. **29**, 1604007 (2017).

[14] W. Luo, F. Shen, C. Bommier, H. Zhu, X. Ji, and L. Hu, Acc. Chem. Res. **49**, 231 (2016).

[15] V. Kapoor, B. Singh, G. Sai Gautam, A. K. Cheetham, and P. Canepa, Chem. Mater. **34**, 3373 (2022).

[16] B. Singh, Z. Wang, S. Park, G. S. Gautam, J.-N. Chotard, L. Croguennec, D. Carlier, A. K. Cheetham, C. Masquelier, and P. Canepa, J. Mater. Chem. A **9**, 281 (2021).

[17] P. R. Kumar, K. Kubota, D. Igarashi, and S. Komaba, J. Phys. Chem. C **125**, 24823 (2021).

[18] L. Mu, L. Ben, Y.-S. Hu, H. Li, L. Chen, and X. Huang, J. Mater. Chem. A **4**, 7141 (2016).

[19] S. Liu, L. Shao, X. Zhang, M. Zhou, Z. Tao, and J. Chen, J. Alloys Compd. **754**, 147 (2018).

[20] S. D. Setzler, K. T. Stevens, N. C. Fernelius, M. P. Scripsick, G. J. Edwards, and L. E. Halliburton, J. Phys.: Condens. Matter **15**, 3969 (2003).

[21] A. Bocchini, C. Eigner, C. Silberhorn, W. G. Schmidt, and U. Gerstmann, Phys. Rev. Mater. **4**, 124402 (2020).

[22] A. Bocchini, U. Gerstmann, and W. G. Schmidt, Phys. Rev. B **105**, 205118 (2022).

[23] M. G. Roelofs, J. Appl. Phys. **65**, 4976 (1989).

[24] N. B. Angert, V. M. Garmash, N. I. Pavlova, and A. V. Tarasov, Sov. J. Quantum Electron. **21**, 426 (1991).

[25] B. Boulanger, I. Rousseau, J. P. Feve, M. Maglione, B. Menaert, and G. Marnier, IEEE J. Quantum Electron. **35**, 281 (1999).

[26] B. Boulanger, M. M. Fejer, R. Blachman, and P. F. Bordui, Appl. Phys. Lett. **65**, 2401 (1994).

[27] G. M. Loiacono, D. N. Loiacono, T. McGee, and M. Babb, J. Appl. Phys. **72**, 2705 (1992).

[28] S. S. Fedotov, N. D. Luchinin, D. A. Aksyonov, A. V. Morozov, S. V. Ryazantsev, M. Gaboardi, J. R. Plaisier, K. J. Stevenson, A. M. Abakumov, and E. V. Antipov, Nat. Commun. **11**, 1484 (2020).

[29] N. S. Katorova, S. S. Fedotov, D. P. Rupasov, N. D. Luchinin, B. Delattre, Y.-M. Chiang, A. M. Abakumov, and K. J. Stevenson, ACS Appl. Energy Mater. **2**, 6051 (2019).

[30] H. Tan, X. Du, J.-Q. Huang, and B. Zhang, Chem. Commun. **55**, 11311 (2019).

[31] S. S. Fedotov, A. S. Samarin, and E. V. Antipov, J. Power Sources **480**, 228840 (2020).

[32] S. S. Fedotov, N. R. Khasanova, A. S. Samarin, O. A. Drozhzhin, D. Batuk, O. M. Karakulina, J. Hadermann, A. M. Abakumov, and E. V. Antipov, Chem. Mater. **28**, 411 (2016).

[33] K. Chihara, A. Katogi, K. Kubota, and S. Komaba, Chem. Commun. **53**, 5208 (2017).

[34] M. Galceran, J. Rikarte, M. Zarrabeitia, M. C. Pujol, M. Aguiló, and M. Casas-Cabanas, ACS Appl. Energy Mater. **2**, 1923 (2019).

[35] G. Bhar, P. Kumbhakar, A. Chaudhary, and U. Chatterjee, Pramana **53**, 321 (1999).

[36] W. R. Bosenberg, L. K. Cheng, and J. D. Bierlein, Appl. Phys. Lett. **65**, 2765 (1994).

[37] J. D. Bierlein, H. Vanherzeele, and A. A. Ballman, Appl. Phys. Lett. **54**, 783 (1989).

[38] O. Khyzhun, V. Bekenev, V. Atuchin, A. Sinelnichenko, and L. Isaenko, J. Alloys Compd. **477**, 768 (2009).

[39] G. M. Loiacono, D. N. Loiacono, J. J. Zola, R. A. Stolzenberger, T. McGee, and R. G. Norwood, Appl. Phys. Lett. **61**, 895 (1992).

[40] S. Neufeld, A. Schindlmayr, and W. G. Schmidt, J. Phys.: Mater. **5**, 015002 (2022).

[41] N. Voronina, J. H. Jo, A. Konarov, J. Kim, and S.-T. Myung, Small **16**, 2001090 (2020).

[42] P. Giannozzi, S. Baroni, N. Bonini, M. Calandra, R. Car, C. Cavazzoni, D. Ceresoli, G. L. Chiarotti, M. Cococcioni, I. Dabo, A. D. Corso, S. de Gironcoli, S. Fabris, G. Fratesi, R. Gebauer, U. Gerstmann, C. Gougoussis, A. Kokalj, M. Lazzeri, L. Martin-Samos *et al.*, J. Phys.: Condens. Matter **21**, 395502 (2009).

[43] P. Giannozzi, O. Andreussi, T. Brumme, O. Bunau, M. B. Nardelli, M. Calandra, R. Car, C. Cavazzoni, D. Ceresoli, M. Cococcioni, N. Colonna, I. Carnimeo, A. D. Corso, S. de Gironcoli, P. Delugas, R. A. DiStasio, A. Ferretti, A. Floris, G. Fratesi, G. Fugallo *et al.*, J. Phys.: Condens. Matter **29**, 465901 (2017).

[44] J. P. Perdew, A. Ruzsinszky, G. I. Csonka, O. A. Vydrov, G. E. Scuseria, L. A. Constantin, X. Zhou, and K. Burke, Phys. Rev. Lett. **100**, 136406 (2008).

[45] V. L. Chevrier, S. P. Ong, R. Armiento, M. K. Y. Chan, and G. Ceder, Phys. Rev. B **82**, 075122 (2010).

[46] F. Zhou, M. Cococcioni, C. A. Marianetti, D. Morgan, and G. Ceder, Phys. Rev. B **70**, 235121 (2004).

[47] E. B. Isaacs, S. Patel, and C. Wolverton, Phys. Rev. Mater. **4**, 065405 (2020).

[48] L. Wang, T. Maxisch, and G. Ceder, Phys. Rev. B **73**, 195107 (2006).

[49] N. Luo, L. Feng, H. Yin, A. Stein, S. Huang, Z. Hou, and D. G. Truhlar, ACS Appl. Mater. Interfaces **14**, 29832 (2022).

[50] M. Cococcioni and N. Marzari, Phys. Rev. Mater. **3**, 033801 (2019).

[51] M. Cococcioni and S. de Gironcoli, Phys. Rev. B **71**, 035105 (2005).

[52] J. P. Perdew, M. Ernzerhof, and K. Burke, J. Chem. Phys. **105**, 9982 (1996).

[53] KTiOAsO$_4$ (KTi[AsO$_4$]O) crystal structure data sheet, Pauling File in Inorganic Solid Phases, Springer Materials (online database), edited by P. Villars (Chief Editor) (Springer, Heidelberg, 2016), https://materials.springer.com/isp/crystallographic/docs/sd_1239147.

[54] A. Baldereschi, Phys. Rev. B **7**, 5212 (1973).

[55] G. Henkelman, B. P. Uberuaga, and H. Jónsson, J. Chem. Phys. **113**, 9901 (2000).

[56] A. Ghosh, S. Pal, and P. Sarkar, J. Phys. Chem. C **126**, 5092 (2022).

[57] V. Krishnamurthy and V. Viswanathan, ACS Energy Lett. **5**, 3330 (2020).

[58] X. Lv, F. Li, J. Gong, J. Gu, S. Lin, and Z. Chen, Phys. Chem. Chem. Phys. **22**, 8902 (2020).

[59] G. Ceder, M. Aydinol, and A. Kohan, Comput. Mater. Sci. **8**, 161 (1997).

[60] G. Yoon, D.-H. Kim, I. Park, D. Chang, B. Kim, B. Lee, K. Oh, and K. Kang, Adv. Funct. Mater. **27**, 1702887 (2017).

[61] A. Urban, D.-H. Seo, and G. Ceder, npj Comput. Mater. **2**, 16002 (2016).

[62] A. Bocchini, S. Neufeld, U. Gerstmann, and W. G. Schmidt, J. Phys.: Condens. Matter **31**, 385401 (2019).

[63] M. E. Arroyo y de Dompablo, A. Van der Ven, and G. Ceder, Phys. Rev. B **66**, 064112 (2002).

[64] D. Adekoya, S. Zhang, and M. Hankel, ACS Appl. Mater. Interfaces **12**, 25875 (2020).